

# Martian cave detection via machine learning coupled with visible light imagery

Thomas H. Watson<sup>\*</sup>, James U.L. Baldini

Department of Earth Sciences, Durham University, DH1 3LE, UK

## ARTICLE INFO

### Keywords:

Caves  
Lava tubes  
Mars  
Convolutional neural network  
Martian caves

## ABSTRACT

Cave entrances on Mars, formed from lava tube collapses, are key to the future exploration of the planet. They represent valuable exploration targets for signs of life and could provide shelter for prospective human endeavours. In this survey, a convolutional neural network (CNN), trained to identify potential cave entrances (PCEs) from images of the Martian surface, is used to locate new potential caves. Five regions were targeted for search, totalling around 1.1% of the Martian surface. **Region A** (latitude:  $-20^{\circ}$  N to  $-8^{\circ}$  N, longitude:  $-120^{\circ}$  E to  $-132^{\circ}$  E, centre:  $-14^{\circ}$  N,  $-126^{\circ}$  E), **Region B** (latitude:  $0^{\circ}$  N to  $-12^{\circ}$  N, longitude:  $-108^{\circ}$  E to  $-120^{\circ}$  E, centre:  $-6^{\circ}$  N,  $-114^{\circ}$  E), **Region C** (latitude:  $0^{\circ}$  N to  $12^{\circ}$  N, longitude:  $-100^{\circ}$  E to  $-112^{\circ}$  E, centre:  $6^{\circ}$  N,  $-106^{\circ}$  E), **Region D** (latitude:  $-28^{\circ}$  N to  $-40^{\circ}$  N, longitude:  $88^{\circ}$  E to  $100^{\circ}$  E, centre:  $-34^{\circ}$  N,  $94^{\circ}$  E) and **Region E** (latitude:  $20^{\circ}$  N to  $32^{\circ}$  N, longitude:  $140^{\circ}$  E to  $152^{\circ}$  E, centre:  $26^{\circ}$  N,  $146^{\circ}$  E). Each region selected either contains a high abundance of previously identified PCEs or is known to contain volcanic surface features. The network identified 61 new and 24 previously identified PCEs out of 10,834 positive outputs (0.78%). This accounted for  $\sim 7.0\%$  of the 341 previously identified PCEs present in the five regions surveyed. Four newly identified PCEs are highlighted as promising candidates for future research, including a very large ( $\sim 700$  m diameter) PCE ('Marvin'; following previous convention, PCEs are informally named for ease of reference (Cushing et al., 2007)), as well as a PCE whose low altitude could enable exploration via remote controlled drone ('Emily'). Twelve PCE-dense sub-regions capable of facilitating rapid exploration were also identified. Of these, sub-region B<sub>2</sub> contains the largest number of PCEs suggesting the most promise for future research. Overall, the network's 0.78% success rate of PCE detection is approximately 37 times more effective than random selection of locations (estimated as a 0.02% chance of detection). This suggests that there is great potential for cave discovery with this method, although improvements in the size and quality of the training dataset are required prior to planet-wide application. Advancements in current exploration technologies are also necessary before confirming any PCE identified as an actual cave entrance.

## 1. Introduction

Remote identification of potential cave entrances (PCEs) is crucial for future direct exploration of caves on Mars. Additionally, Martian caves represent unique opportunities for identifying biosignatures of extra-terrestrial microbial life. Their stable environmental conditions enhance both secondary mineral precipitation and microbial growth (Léveillé and Datta, 2010). On Earth, many caves are found to sustain abundant microbial growth, by providing protection from seasonal climate effects, extreme weather, UV radiation, and the grazing of other organisms (Boston et al., 2001; Barton, 2006). Cave discoveries are also significant for future human exploration of Mars, providing shelter from

a range of harsh surface conditions, such as micrometeoroid impacts, dust storms, extreme temperature variations, and high fluxes of solar radiation (Boston, 2004). Moreover, they provide easy access to geological materials of potential practical and economic value. Therefore, locating Martian caves is more than an academic matter as these findings may yield evidence of life on Mars and/or provide ideal bases for human habitats.

Knowledge of Martian geology has greatly improved over the past 50 years following successful rover and lander missions (Viking (1976–1982); Pathfinder and Sojourner (1997–1997); Opportunity (2004–2018); Spirit (2004–2010); Phoenix (2008–2008); Curiosity (2012–); InSight (2018–2022); Perseverance (2021–); Zhurong (2021–))

<sup>\*</sup> Corresponding author.

E-mail address: [thwatson26@gmail.com](mailto:thwatson26@gmail.com) (T.H. Watson).

<https://doi.org/10.1016/j.icarus.2024.115952>

Received 25 July 2023; Received in revised form 6 January 2024; Accepted 7 January 2024

Available online 9 January 2024

0019-1035/© 2024 The Authors. Published by Elsevier Inc. This is an open access article under the CC BY license (<http://creativecommons.org/licenses/by/4.0/>).

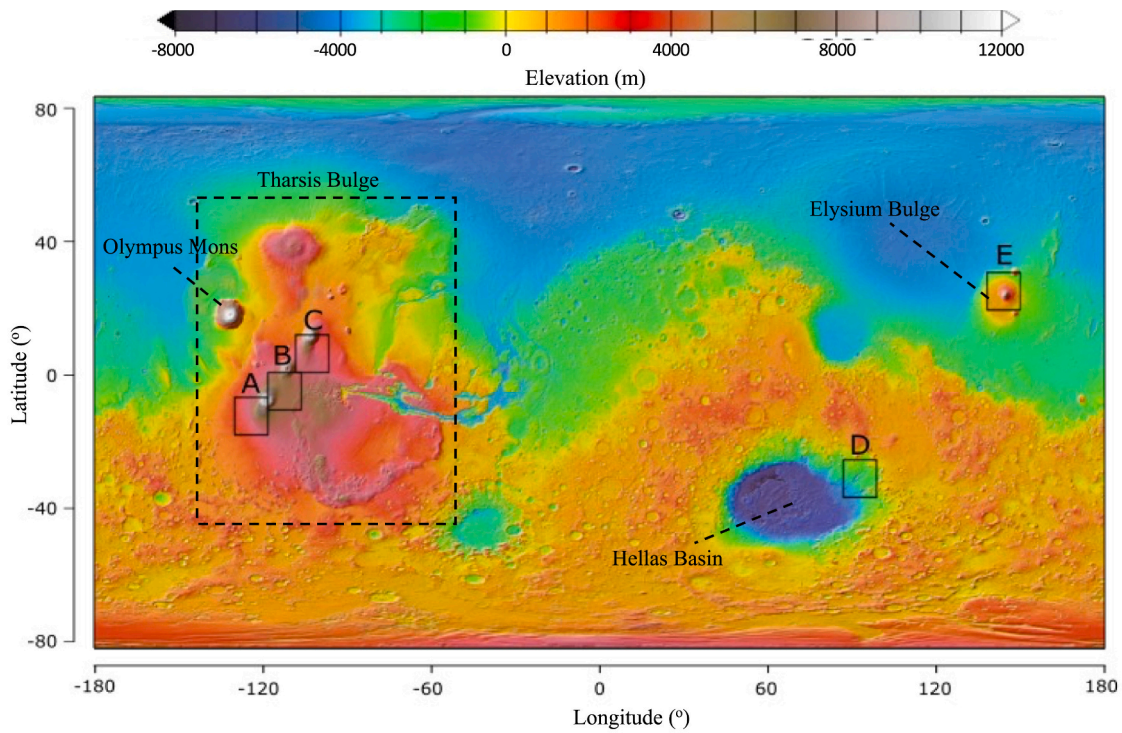


**Fig. 1.** Elevation map of Martian surface with five survey regions highlighted. The Tharsis and Elysium Bulges and the Hellas Basin are also highlighted. Map created using MOLA Shaded relief/ colorized digital elevation map from JMARS.

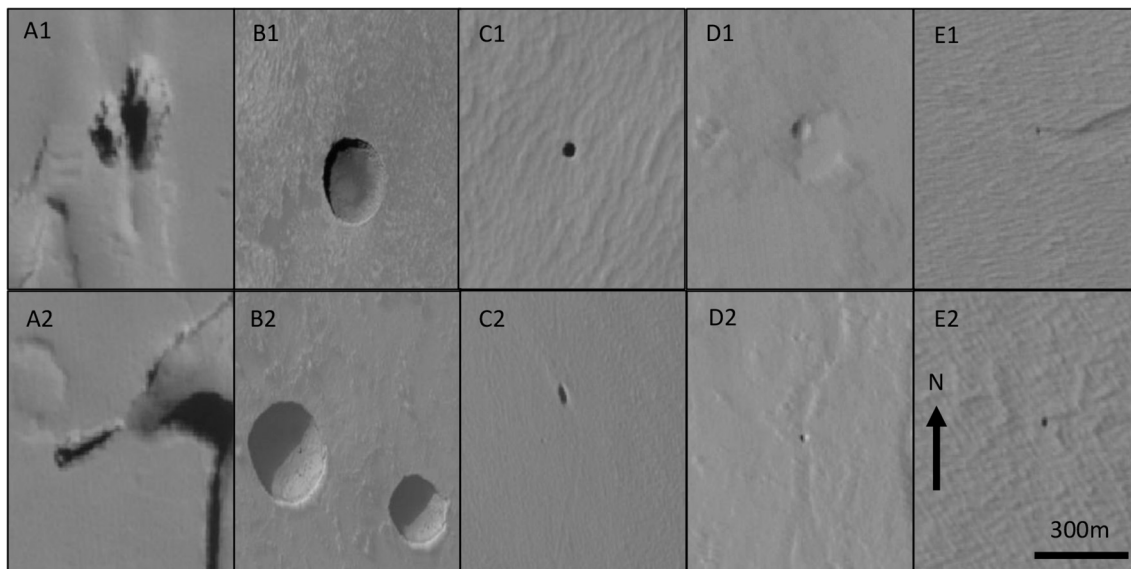


**Fig. 2.** Examples of PCEs and their assigned category from the Mars Global Candidate cave Catalogue (MGC<sup>3</sup>) (Cushing, 2015). Examples include deep irregular pits (A1&A2), atypical pit craters (APCs) (B1&B2), skylights (C1&C2), small rimless pits (SRPs) (D1&D2) and pinholes (E1&E2). This does not include all categories of PCE included in the MGC<sup>3</sup>. All images were captured at the same scale and orientation, on the CTX Global Mosaic (NASA/JPL/MSSS/The Murray Lab.).

as well as numerous advancements in satellite imaging capabilities (e.g., 2001 Mars Odyssey; Mars Reconnaissance Orbiter; Emirates Mars Mission). Despite this, the obvious accessibility restrictions greatly complicate geological study, limiting confirmation of theories. Current research aims to refine our understanding by improving the mobility of Martian robotics (e.g., Petrovsky et al., 2022), expanding surface exploration via flight (e.g., Biswal M and Kumar, 2021), and ultimately achieving crewed missions to the planet (e.g., Aprovitola et al., 2022; Dede, 2022).

Over its 4.6 Gyr history, Mars has experienced extensive volcanism, likely only ceasing a few tens of millions of years ago (Neukum et al., 2004). Much of this volcanic record is preserved due to low rates of erosion and a lack of plate tectonics, meaning that no recycling of the lithosphere has occurred (Carr, 1973). This lack of plate tectonics makes Martian volcanoes analogous to terrestrial mid-plate volcanoes on Earth, possibly forming over stationary mantle plumes (Carr and Head III, 2010).

The highest concentrations of volcanoes on Mars are found in the

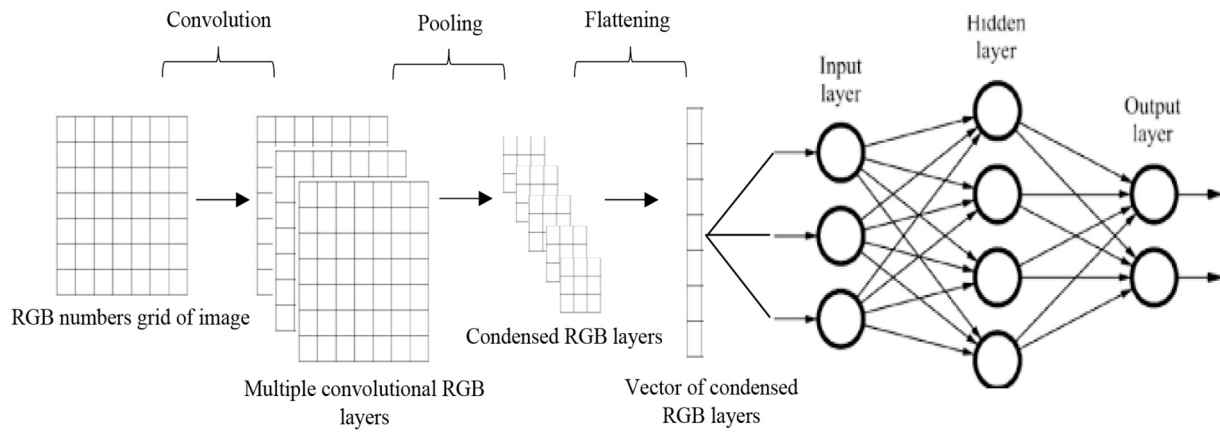


Fig. 3. Visualisation of a convolutional neural network (CNN). Image data, represented as an empty number matrix (left), is condensed to a column vector, as it moves from left to right. This vector is then inputted into the connected network (right) before being outputted with an associated classification. (Image modified from Saha, 2018).

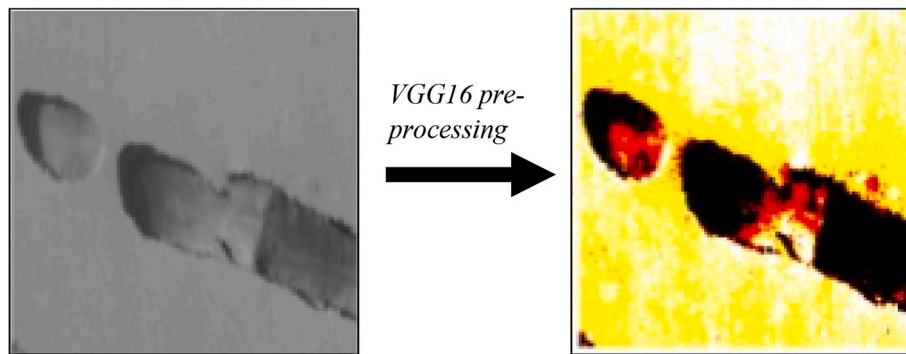


Fig. 4. Example of an MGC<sup>3</sup> PCE image before (left) and after (right) VGG16 pre-processing. All images underwent VGG16 pre-processing prior to being inputted to the network.

Model: "sequential"

Layer (type)	Output Shape	Param #
conv2d (Conv2D)	(None, 224, 224, 32)	896
max_pooling2d (MaxPooling2D)	(None, 112, 112, 32)	0
conv2d_1 (Conv2D)	(None, 112, 112, 64)	18496
max_pooling2d_1 (MaxPooling2D)	(None, 56, 56, 64)	0
flatten (Flatten)	(None, 200704)	0
dense (Dense)	(None, 2)	401410

=====  
 Total params: 420,802  
 Trainable params: 420,802  
 Non-trainable params: 0  
 =====

None

Fig. 5. Diagram detailing CaveFinder's architecture.

**Table 1**  
Performance metrics of training versus validation accuracy after six rounds of training with augmented datasets. The mean accuracy after each round is also given. The best performing round (achieved by CaveFinder), in terms of both training and validation accuracy, is highlighted in green.

Training Round	Training Accuracy	Validation Accuracy	Average Accuracy
1	1.0000	0.8333	0.91665
2	0.9540	0.8889	0.92145
3	0.9829	0.8889	0.9359
4 (CaveFinder)	0.9955	0.9375	0.9665
5	0.9738	0.9236	0.9487
6	0.8847	0.8145	0.8496

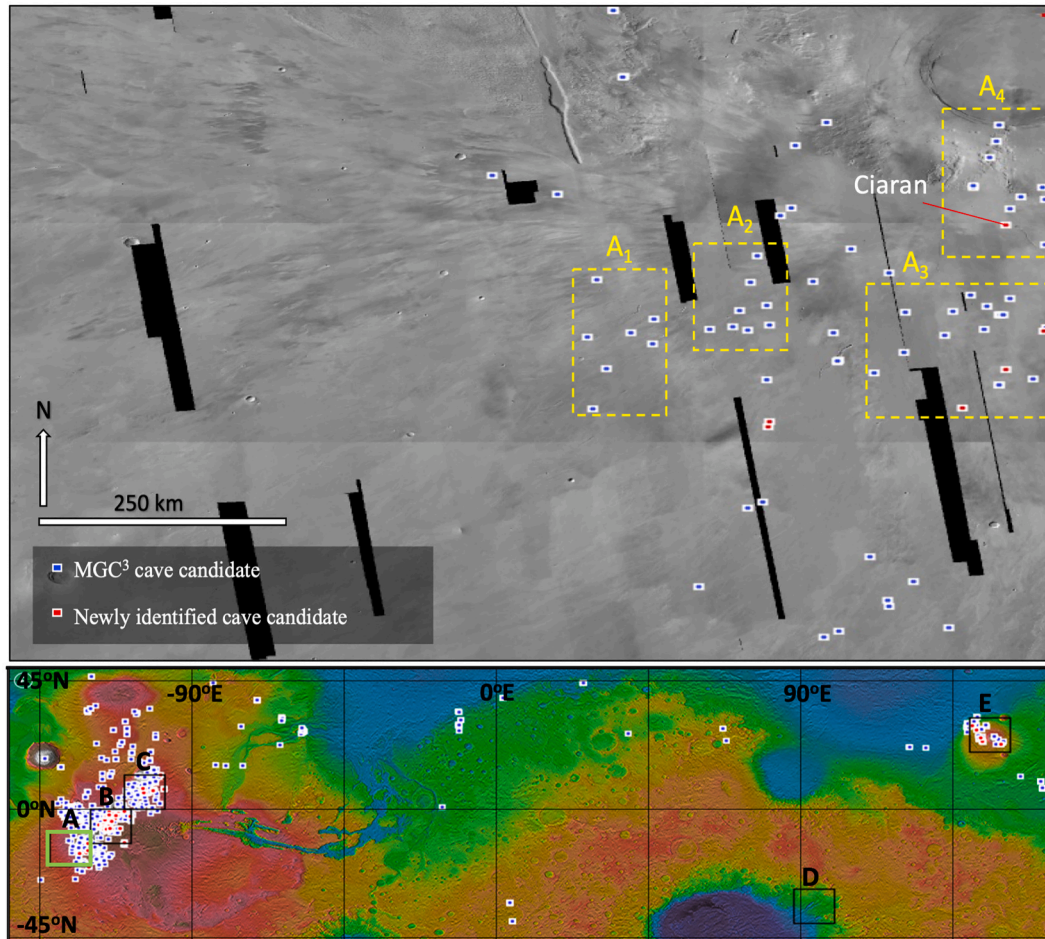


**Fig. 6.** *Top panel:* Location of all known PCEs in region A (latitude:  $-20^{\circ}$  N to  $-8^{\circ}$  N, longitude:  $-120^{\circ}$  E to  $-132^{\circ}$  E), visualised on the CTX Global Mosaic (NASA/JPL/MSSS/The Murray Lab.). PCE-dense subregions are outlined in yellow. *Bottom panel:* Location of all known PCEs between  $45^{\circ}$  N and  $-45^{\circ}$  N shown on a colourised elevation map of Mars. Includes the locations of all the survey regions, with region A highlighted green. PCEs identified in this study are in red whereas those included in the MGC<sup>3</sup> are shown in blue. (For interpretation of the references to colour in this figure legend, the reader is referred to the web version of this article.)

Tharsis and Elysium regions (Fig. 1). The Tharsis region covers almost 25% of the planet’s surface and was primarily accumulated during the Noachian (4.1–3.7 billion years ago) (Phillips, 2001). The geology of this region consists mostly of basaltic deposits from shield volcanoes (Rossi and Van Gasselt, 2010). The comparatively smaller Elysium province is located east of Tharsis (Fig. 1) and contains three major shield volcanoes: Elysium Mons, Hecates Tholus, and Albor Tholus. Both regions experienced considerable lava flows which, due to the relatively reduced gravity, have travelled up to six times further than those found on Earth (Wilson and Head, 1994). This has created many volcanic surface features, possibly including extensive cave systems in the form of lava

tubes.

Lava tubes are formed when a roofed conduit of flowing lava is drained or plugged, leaving behind a hollow ‘tube’ beneath the surface (Gunn, 2004). On Earth, lava tubes vary from only a few meters to tens of kilometres, such as the 65 km-long Kazumura Cave in Hawaii (Allred and Allred, 1997). They can form at depths of a few centimetres to tens of metres beneath the surface, with typical tube diameters ranging between 0.5 and 30 m (Sauro et al., 2020). During prolonged eruptions, several tubes often merge focusing lava flow along a primary path. This focused flow enlarges and entrenches the conduit due to its high thermal erosion potential (Kemp, 2019) leaving behind an open, trench-like

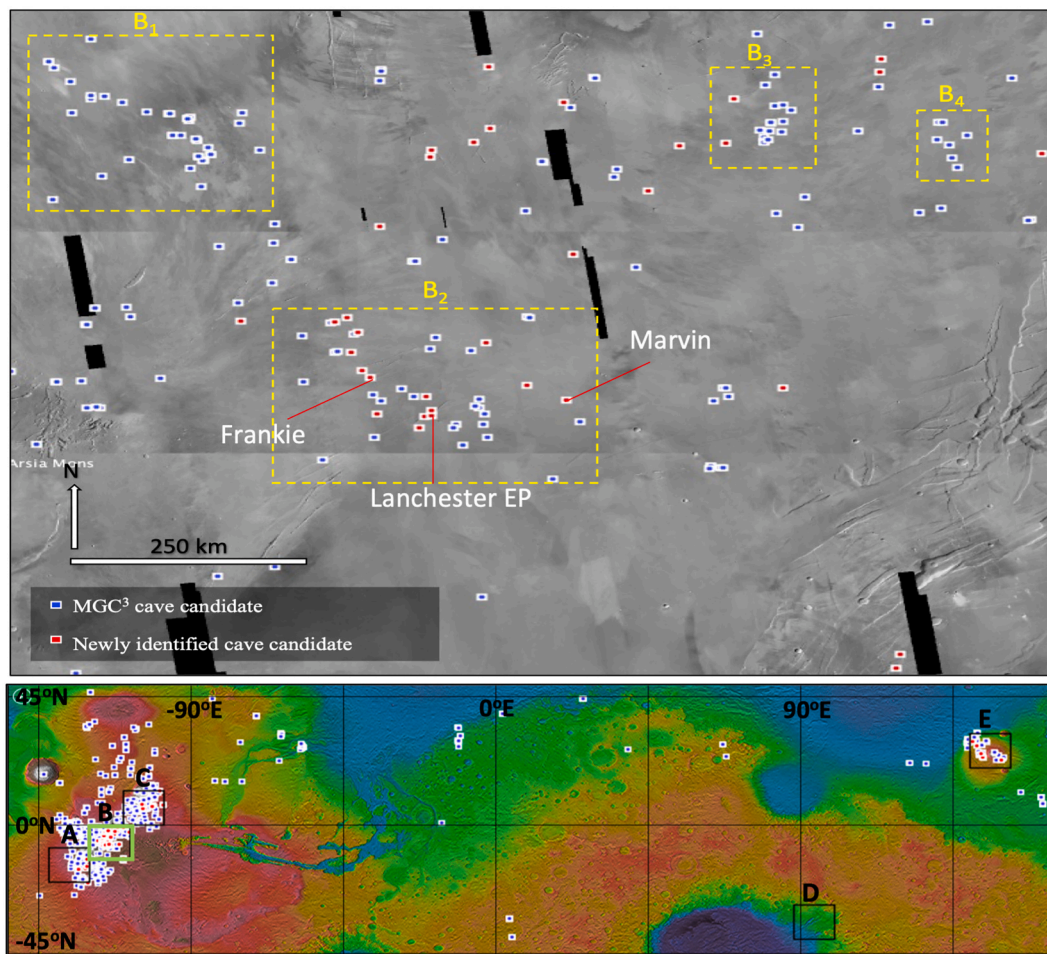


**Fig. 7.** *Top panel:* Location of all known PCEs in region B (latitude:  $0^{\circ}$  N to  $-12^{\circ}$  N, longitude:  $-108^{\circ}$  E to  $-120^{\circ}$  E), visualised on the CTX Global Mosaic (NASA/JPL/MSSS/The Murray Lab.). PCE-dense subregions are outlined in yellow. *Bottom panel:* Location of all known PCEs between  $45^{\circ}$  N and  $-45^{\circ}$  N shown on a coloured elevation map of Mars. Includes the locations of all the survey regions, with region B highlighted green. PCEs identified in this study are in red whereas those included in the MGC<sup>3</sup> are shown in blue. (For interpretation of the references to colour in this figure legend, the reader is referred to the web version of this article.)

tube.

Ceiling collapses represent the main surface expression of lava tubes and can occur due to flow overpressure during formation or because of gravitational burden when the tube drains. Ceiling collapses often occur in chains along the length of the cave system. Two commonly identified collapse types on Earth are proper ‘jameos’ which involve the collapse of the whole tube width, forming steep detrital slopes, and skylights, where the opening is much smaller than the width of the tube below (Sauro et al., 2020). Lava tubes and their associated ceiling collapses have been studied extensively on Earth and may also exist on other planetary bodies such as the Moon and Mars (Cushing, 2012; Haruyama et al., 2009; Leone, 2014; Wagner and Robinson, 2014).

Features that may be associated with Martian caves have been observed for the past 60 years, often recorded as sinuous rilles and sinkholes in volcanic terrains (Quaide and Oberbeck, 1969). Because of the logistical issues associated with exploration, surface geomorphological features alone imply their existence. Consequently, the potential entrances are referred to as ‘PCEs’.

Given that the gravitational field on Mars is 37% of that on Earth, the forces acting on the roofs of Martian lava tubes are comparatively weaker. This has allowed cave entrances to form significantly larger diameters than terrestrial equivalents, with some reaching up to 400 m (Sauro et al., 2020). The increased size of these skyward facing entrances, coupled with the lack of vegetation, facilitate visible detection of PCEs via satellite imagery (e.g., Cushing et al., 2007; Cushing et al., 2015; Hodges and Moore, 1994). Thermal signatures are also used for

cave detection on Mars; however, the ability to identify caves from temperature variations alone is challenging (Jung et al., 2014).

Most detections of Martian PCEs come from a manual review of visible satellite imagery. The Mars Global Candidate Cave Catalogue (MGC<sup>3</sup>) contains the coordinates and brief descriptions of over one thousand identified PCEs on Mars (Cushing, 2015). Entries were identified from images taken by the Mars Reconnaissance Orbiter’s (MRO) Context Camera (CTX) and High-Resolution Imaging Science Experiment (HiRISE) cameras. Only sky-facing entrances larger than 25 m across are identifiable with the resolution of these cameras (Murchie et al., 2007). Most PCEs were recorded as either skylights or a type of atypical pit crater (APCs), equivalent to proper ‘jameos’ (Fig. 2). Manual review of satellite imagery for Martian cave detection is far from efficient on a planet-wide scale, due to the time constraints associated with reviewing such a large dataset (Cushing, 2015). Machine learning presents an intriguing solution to this problem, reducing the dataset to only include imagery computationally determined to contain a PCE.

Here, our primary objective is to extend the existing database of PCEs on Mars by using a convolutional neural network trained to identify PCEs in visible light imagery (VLI) of the Martian surface.

## 2. Methods

### 2.1. Machine learning – neural networks

Machine learning is increasingly utilised for the remote classification

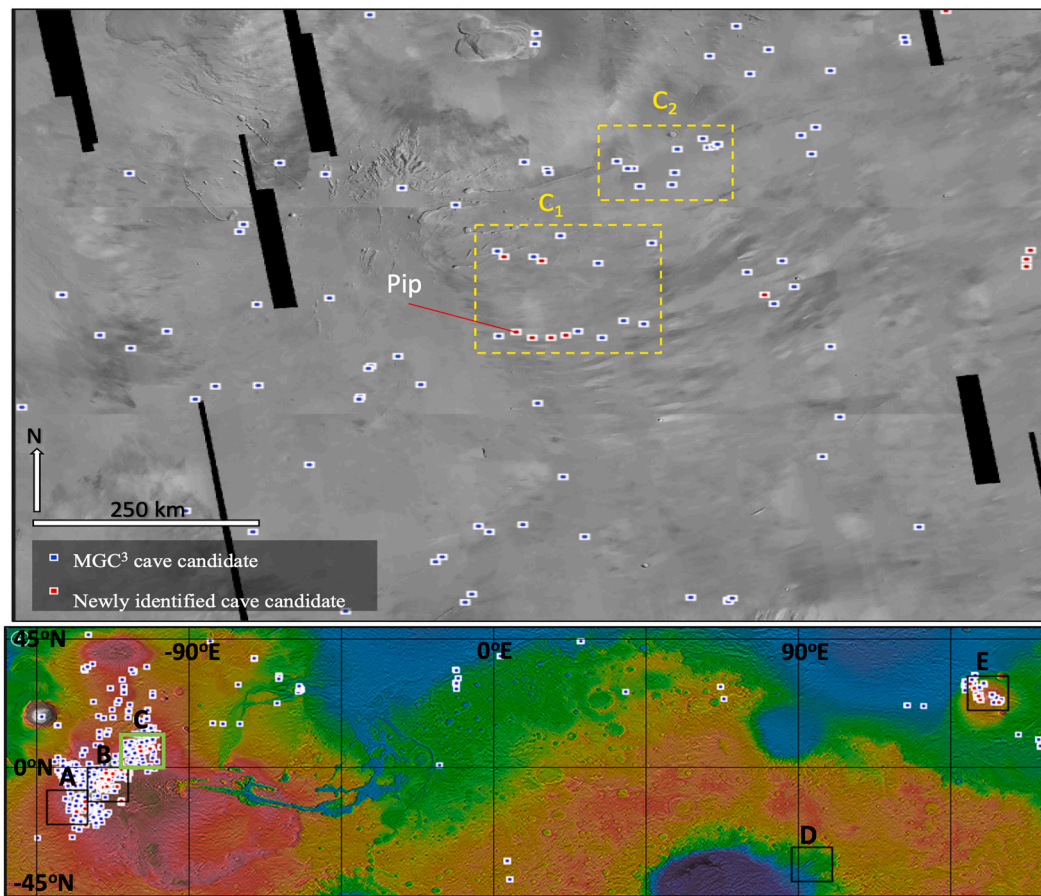


**Fig. 8.** *Top panel:* Location of all known PCEs in region C (latitude:  $0^{\circ}$  N to  $12^{\circ}$  N, longitude:  $-100^{\circ}$  E to  $-112^{\circ}$  E), visualised on the CTX Global Mosaic (NASA/JPL/MSSS/The Murray Lab.). PCEs-dense subregions are outlined in yellow. *Bottom panel:* Location of all known PCEs between  $45^{\circ}$  N and  $-45^{\circ}$  N shown on a colourised elevation map of Mars. Includes the locations of all the survey regions, with region C highlighted green. PCEs identified in this study are in red whereas those included in the MGC<sup>3</sup> are shown in blue. (For interpretation of the references to colour in this figure legend, the reader is referred to the web version of this article.)

of Mars' geological features (e.g., Nagle-McNaughton et al., 2020; Palafox et al., 2017; Shozaki et al., 2022; Wang et al., 2018). Convolutional neural networks (CNNs) are a popular choice for this as, compared to other classifiers, they have the best performance metrics for image recognition (Graham, 2015). CNNs are loosely inspired by studies of central nervous systems in mammals (O'Shea and Nash, 2015), and comprise layers of interconnected neurons (nodes) that transfer signals (fire) when certain inputs are received (Fig. 3). Each node consists of a weight and a bias, randomly assigned prior to training. To input a signal to the CNN, images first undergo convolution, padding and pooling, which extract the image's dominant features to save computational time (Saha, 2018). The images are then 'flattened' to their corresponding red-green-blue (RGB) colour value vector (Fig. 3). When a signal (for PCE images, an RGB vector) arrives at a node, it is multiplied by the node's weight (for vector inputs, the dot product is taken) and then summed with the bias. An activation function is then applied, commonly ReLU (Rectified Linear Unit), which prevents the node from firing if the output is negative, and fires with increasing confidence for increasingly positive outcomes. For binary classifiers, once the final layer of the network is reached, one-hot encoding classifies the output as a value between one and zero.

CNN training consists of loading known inputs with their corresponding classifications (labels) into the network in batches. The colour and pixel distribution of a given image are used by the network to predict if a PCE is present. After each batch of predictions, an optimiser function adjusts each node's weight and bias depending on how 'wrong' the predictions were, calculated using a loss function. This process is known as loss minimization and over time improves the network's

accuracy. CNNs trained to recognise Martian surface features, such as craters, have achieved accuracies in excess of 90% (Palafox et al., 2017). However, when handling large datasets, this still produces a significant number of incorrect predictions, somewhat limiting their application.

## 2.2. Survey regions

CTX satellite imagery of Mars' surface was loaded as TIFF image files with several layers of zoom. A trade-off exists between the survey size and image resolution when selecting the optimal zoom level to attain images for the neural network. A zoom level of 32,768 Pixel Per Degree (PPD) was chosen to optimise the number of resolved MGC<sup>3</sup> PCEs. This zoom level would require over 136 million input images to cover the entire Martian surface.

To increase the chance of PCE detection, five locations (referred to herein as regions A, B, C, D, and E), either containing high concentrations of MGC<sup>3</sup> PCEs or volcanic surface features, were chosen for the survey dataset. Each location surveyed a  $12^{\circ} \times 12^{\circ}$  area, totalling around 1.1% of the Martian surface (Fig. 1).

**Regions A, B, and C** are located in the Tharsis Bulge, with the large volcano, Olympus Mons, situated around 1500 km to the NE (Fig. 1). **Region A** (latitude:  $-20^{\circ}$  N to  $-8^{\circ}$  N, longitude:  $-120^{\circ}$  E to  $-132^{\circ}$  E, centre:  $-14^{\circ}$  N,  $-126^{\circ}$  E) contains 68 MGC<sup>3</sup> PCEs. The volcano Arsia Mons is located in the region's NE corner. **Region B** (latitude:  $0^{\circ}$  N to  $-12^{\circ}$  N, longitude:  $-108^{\circ}$  E to  $-120^{\circ}$  E, centre:  $-6^{\circ}$  N,  $-114^{\circ}$  E) contains 152 MGC<sup>3</sup> PCEs. The Arsia Mons volcano is located in the region's SW corner and the Pavonis Mons volcano is located in the North. The smaller volcanoes Ulysses Tholus and Biblis Tholus are located to the NE. **Region C**

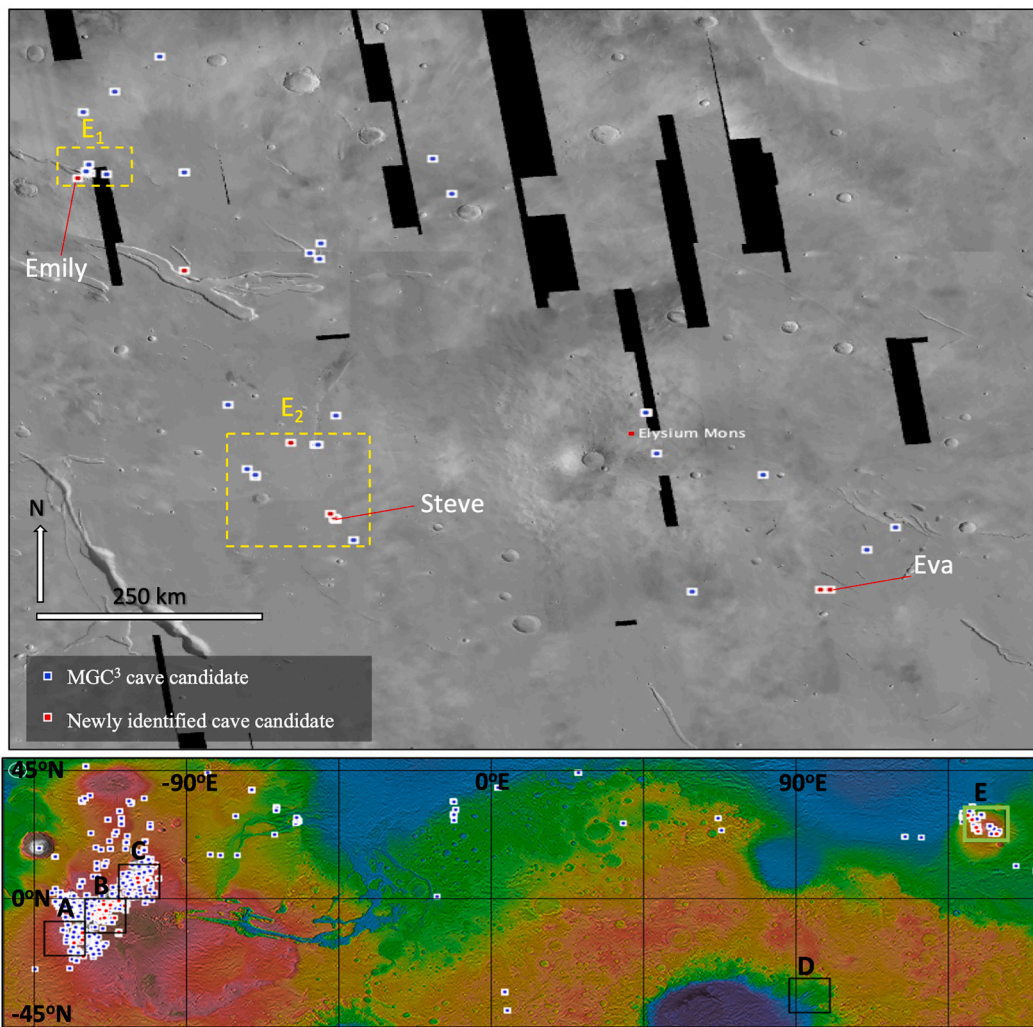


Fig. 9. *Top panel*: Location of all known PCEs in region E (latitude:  $20^{\circ}$  N to  $32^{\circ}$  N, longitude:  $140^{\circ}$  E to  $152^{\circ}$  E), visualised on the CTX Global Mosaic (NASA/JPL/MSSS/The Murray Lab.). PCE-dense subregions are outlined in yellow. *Bottom panel*: Location of all known PCEs between  $45^{\circ}$  N and  $-45^{\circ}$  N shown on a colourised elevation map of Mars. Includes the locations of all the survey regions, with region E highlighted green. PCEs identified in this study are in red whereas those included in the MGC<sup>3</sup> are shown in blue. (For interpretation of the references to colour in this figure legend, the reader is referred to the web version of this article.)

(latitude:  $0^{\circ}$  N to  $12^{\circ}$  N, longitude:  $-100^{\circ}$  E to  $-112^{\circ}$  E, centre:  $6^{\circ}$  N,  $-106^{\circ}$  E) contains 89 MGC<sup>3</sup> PCEs and covers the volcano Ascraeus Mons' southern slope. The smaller Tharsis Tholus volcano is located to the NE. **Region D** (latitude:  $-28^{\circ}$  N to  $-40^{\circ}$  N, longitude:  $88^{\circ}$  E to  $100^{\circ}$  E, centre:  $-34^{\circ}$  N,  $94^{\circ}$  E) is located east of the Hellas Basin. There are no MGC<sup>3</sup> PCEs present, but the volcano Tyrrhenus Mons is located to the NE. Lava tubes are detectable in this region, as well as signs of fluvial and glacial activity, increasing the possibility of life existing in water-related minerals in any PCEs detected (Husseini et al., 2009). **Region E** (latitude:  $20^{\circ}$  N to  $32^{\circ}$  N, longitude:  $140^{\circ}$  E to  $152^{\circ}$  E, centre:  $26^{\circ}$  N,  $146^{\circ}$  E) is located in the Elysium Bulge and contains 32 MGC<sup>3</sup> PCEs. The region is centred around the Elysium Mons volcano with the smaller Albor Tholus and Hecates Tholus volcanoes to the SE and NE of the region respectively.

### 2.3. Training data

Three datasets are required to train a neural network: training, validation, and test. Each dataset requires an equal number of positive (containing a PCE) and negative (not containing a PCE) images. Positive images for these datasets were collected using MGC<sup>3</sup> PCE coordinates. Training images were collected on JMARS (a GIS tool used to visualise remote sensing data retrieved from a variety of planetary bodies

(Christensen et al., 2022)) using a python automation script, coded to input coordinates from the MGC<sup>3</sup> and take a screenshot of the resulting PCE image (see Supplementary Information). The CTX Global Mosaic (Dickson et al., 2018) was used to generate the images of the PCEs on JMARS, with screenshots taken at the required 32,768 PPD. Overall, the dataset consisted of 1065 images of MGC<sup>3</sup> PCEs which were randomly subdivided into 851 training images (80%), 160 validation images (15%), and 54 test images (5%).

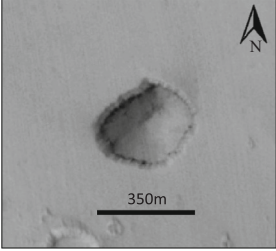
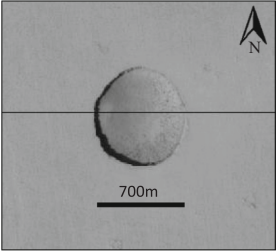
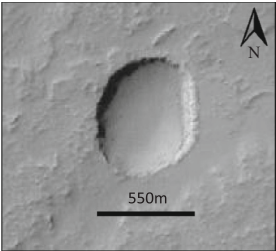
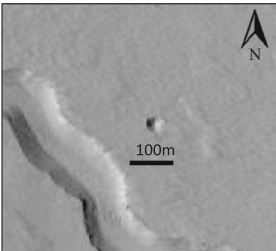
Negative images were obtained using 1065 randomly generated coordinates of the Martian surface. The same python script, at 32,768 PPD on the CTX Global Mosaic, was used to collect the images in JMARS. Each image was manually checked to confirm no PCE was present, before the group was subdivided into the same ratios as the positive images.

### 2.4. Data augmentation

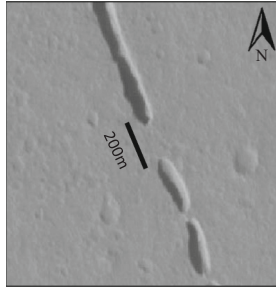
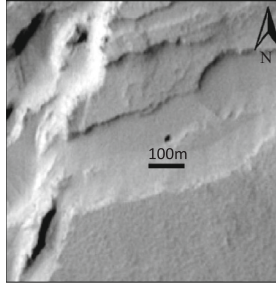
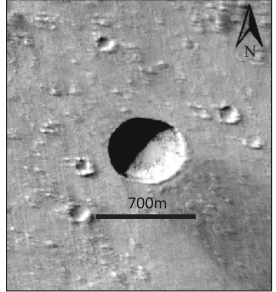
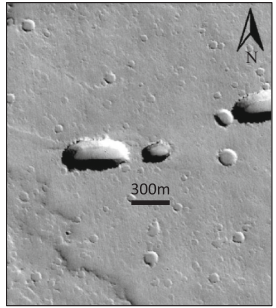
Visual analysis of the training datasets found that some of the positive images contained no visible PCE, because either the zoom level used was ineffective at resolving small PCEs or because of slight inaccuracies in the coordinates provided in the MGC<sup>3</sup>. These images were removed from the dataset. The reduced dataset contained equal numbers of positive and negative images, each with 283 training, 53 validation, and

**Table 2**

Example images of newly identified PCEs from this survey, highlighting the variety of PCE types identified. Informal names are assigned for ease of reference. Visualised on the CTX Global Mosaic (NASA/JPL/MSSS/The Murray Lab.).

PCE Image	Description
	<p>Region: E (Elysium Province)                      Coordinates: 140.871° E, 29.194° N                      Classification: Atypical pit crater                      MOLA elevation: -1020 m                      Informal name: Emily</p>
	<p>Region: B (Tharsis Bulge)                      Coordinates: 245.472° E, -6.004° N                      Classification: Atypical pit crater                      MOLA elevation: 7330 m                      Informal name: Marvin</p>
	<p>Region: B (Tharsis Bulge)                      Coordinates: 244.143° E, -6.636° N                      Classification: Atypical pit crater                      MOLA elevation: 7806 m                      Informal name: Frankie</p>
	<p>Region: C (Tharsis Bulge)                      Coordinates: 255.851° E, 5.589° N                      Classification: Small rimless pit                      MOLA elevation: 5745 m                      Informal name: Pip</p>

**Table 2 (continued)**

PCE Image	Description
	<p>Region: E (Elysium Province)                      Coordinates: 143.836° E, 23.705° N                      Classification: Pit end and irregular atypical pit craters                      MOLA elevation: 1385 m                      Informal name: Steve</p>
	<p>Region: B (Tharsis Bulge)                      Coordinates: 244.85° E, -7.316° N                      Classification: Pinhole                      MOLA elevation: 7504 m                      Informal Name: Lanchester EP</p>
	<p>Region: A (Tharsis Bulge)                      Coordinates: 239.476° E, -12.047° N                      Classification: Atypical Pit Crater                      MOLA elevation: 11125 m                      Informal Name: Ciaran</p>
	<p>Region: E (Elysium Province)                      Coordinates: 149.499° E, 22.563° N                      Classification: Irregular pit                      MOLA elevation: 1751 m                      Informal Name: Eva</p>

18 test images.

Data augmentation was used to artificially increase the size of this reduced dataset to prevent overfitting, a problem that occurs when a neural network performs well on the training dataset but poorly on larger datasets. The positive dataset was duplicated three times and



**Table 3**

Total area of each PCE-dense subregion and the number of PCEs they contain.

Subregion	Area (km <sup>2</sup> )	Number of MGC <sup>3</sup> PCEs	Number of newly identified PCEs	Total number of PCEs	Coordinates (longitude range, latitude range)
A <sub>1</sub>	12,000	7	0	7	(-125.5° E to -124.5° E), (-13° N to -15.5° N)
A <sub>2</sub>	5500	8	0	8	(-124° E to -123° E), (-12.5° N to -14° N)
A <sub>3</sub>	16,00	16	5	21	(-122.5° E to -120° E), (-13° N to -15.5° N)
A <sub>4</sub>	9000	10	2	12	(-121.5° E to -120° E), (-10° N to -12.5° N)
B <sub>1</sub>	29,000	30	0	30	(-120° E to -117° E), (-0° N to -3.5° N)
B <sub>2</sub>	30,000	27	16	43	(-117° E to -113° E), (-5.5° N to -8.5° N)
B <sub>3</sub>	6500	13	2	15	(-112° E to -110.5° E), (-1° N to -3° N)
B <sub>4</sub>	2000	7	0	7	(-109.5° E to -108.5° E), (-2° N to -3° N)
C <sub>1</sub>	17,500	10	6	16	(-104.5° E to -102.5° E), (7.5° N to 5° N)
C <sub>2</sub>	5000	11	0	11	(-103° E to -101.5° E), (9.5° N to 8° N)
E <sub>1</sub>	400	4	1	5	(140.5° E to 141.5° E), (29.5° N to 29° N)
E <sub>2</sub>	8000	6	4	10	(142.5° E to 144.5° E), (25° N to 23° N)

inputted into a python script which randomly rotated images in the range of 360°, flipped images horizontally and vertically, and zoomed images in the range of 110–150% (see Supplementary Information). This quadrupled the positive dataset's size to 1416 images. The negative image dataset's size was increased by generating 1416 random coordinates and re-running the python automation script to collect non-PCE images. Using image augmentation to increase the dataset beyond this size had no positive effect on the network's performance, a common problem when augmenting a small dataset (Mikołajczyk and Grochowski, 2018). Ultimately, the positive and negative datasets each contained 1132 training, 212 validation, and 72 test images.

All images also underwent VGG16 pre-processing before being inputted into the network (Fig. 4). VGG16 is a state-of-the-art 16-layer CNN, trained on images belonging to over 1000 classes (Simonyan and Zisserman, 2014). The pre-processing function converts each image to a fixed 224 × 224 RGB image, before subtracting the mean RGB value computed on the training set from each pixel. This helps to increase training speed and accuracy by centring the intensities at zero.

## 2.5. Network structure

A sequential model, built using the Keras Machine Learning Library (Chollet, 2015), was trained using the training dataset. The network consists of 420,802 trainable parameters and contains only two hidden layers (Fig. 5). Compared to the 138 million trainable parameters in the VGG16, the network is relatively small. However, VGG16 is trained to identify over 1000 different image categories, whereas only two categories are required for PCE detection (PCE and no PCE). Hence, fewer trainable parameters are required, which helps to increase computational speed. The relatively low complexities of the input images reduces the number of hidden layers required, further saving computational time.

## 2.6. Overfitting

Training was conducted in six rounds to assess the data augmentation's impact on the network's performance. The first training round consisted of the unaugmented training dataset, and was followed by five accumulative rounds using the augmented data. Data for each round consisted of 566 training and 106 validation images, which were loaded into the network in batches of 10 over 10 epochs. The network's performance was assessed after each epoch.

For training round one, the validation accuracy was significantly lower than the training accuracy, indicating that overfitting had occurred (Muralidhar, 2021) (Table 1). Overfitting decreased until training round four, at which point the average accuracy also began to decrease. Hence, model four was chosen as the most optimal network for PCE detection and is referred to as 'CaveFinder' from here onwards.

## 2.7. Survey data

Following CNN training, survey data was loaded into the network for PCE detection. Each individual survey area (Fig. 1) comprised 36 CTX Global Mosaic tiles, each covering 2° × 2° of the Martian surface. To achieve the required 32,768 PPD image resolution, each tile was further split into 8649 images, using a python script (see Supplementary Information). Overall, the survey dataset consisted of 1,556,820 images, inputted into the network in 180 batches. This dataset also underwent VGG16 pre-processing, however, did not undergo any other form of image augmentation prior to input.

## 3. Results

### 3.1. Cave verification criteria

CaveFinder was coded to output the centre coordinates and image of each positive result detected (Supplementary Table 1). Positive outputs from CaveFinder were reviewed manually to confirm that a PCE was indeed present. For images deemed likely to contain a PCE, the corresponding coordinates were inputted into JMARS to further analyse the surrounding area. Typical lava tube collapse characteristics, such as having flat overhanging rims with no ejecta patterns (see Fig. 2), were used to initially identify PCEs. Further analysis evaluated possible connections to lava tubes and other MGC<sup>3</sup> PCEs.

### 3.2. Output from network

In total CaveFinder produced 10,834 positive detections. Following visual cross-checking, only 85 positive outputs were deemed true positives (0.78%). Of these, 24 contained an MGC<sup>3</sup> PCE, accounting for 7.04% of the 341 MGC<sup>3</sup> PCEs within regions A-E. After further review of the outputs, twelve subregions with particularly high abundances of PCEs were also identified.

**Region A:** CaveFinder output 2481 positive PCE detections from region A, however, only 11 were deemed true positives (0.44%). Of

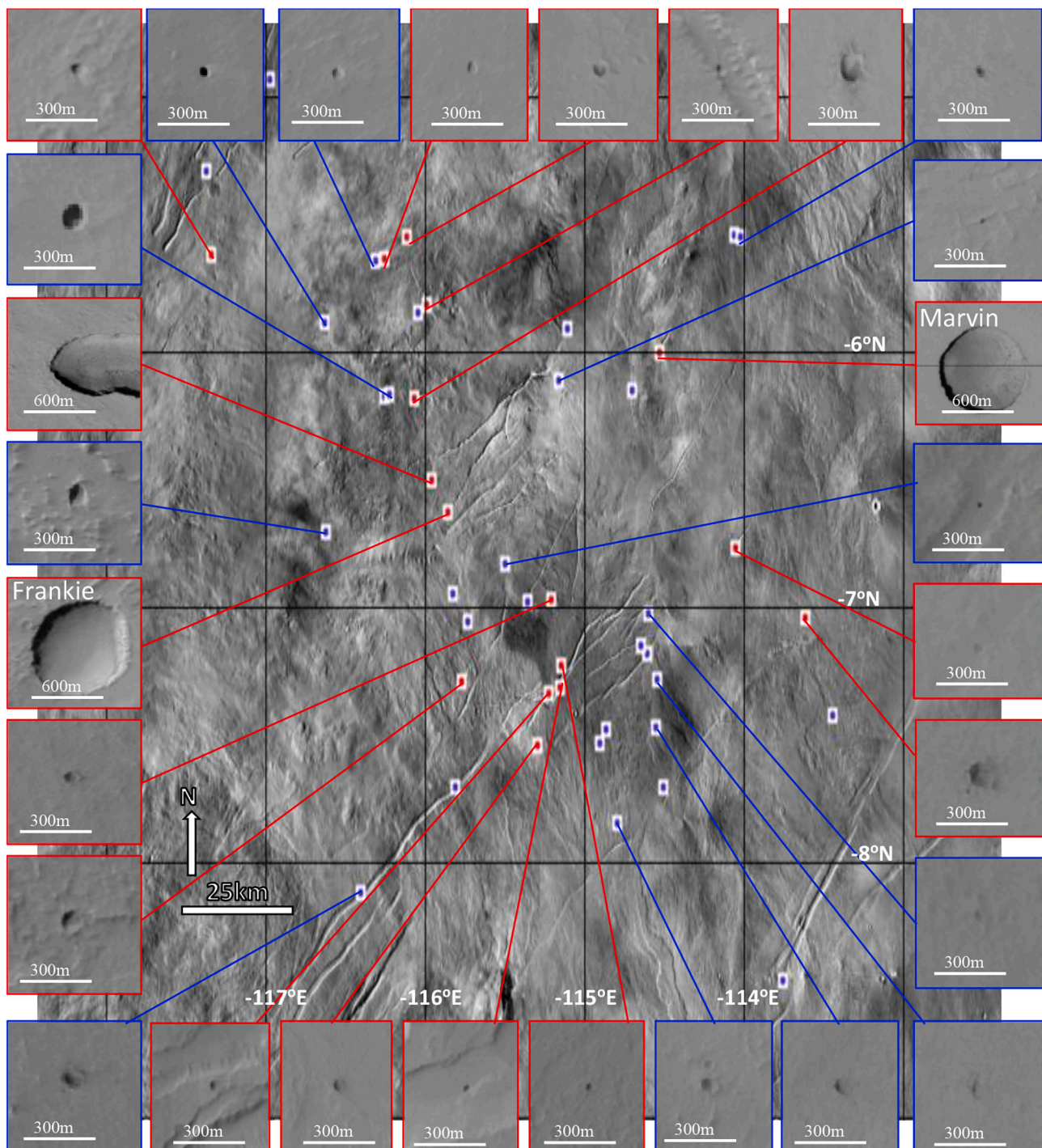


**Fig. 10.** Close up of PCE-dense subregion B<sub>2</sub> (Fig. 7). MGC<sup>3</sup> PCEs are highlighted in blue, whereas newly identified PCEs from this study are highlighted in red. Close up images of all the newly identified PCEs and examples of some MGC<sup>3</sup> PCEs are included. Visualised on the CTX Global Mosaic (NASA/JPL/MSSS/The Murray Lab.). (For interpretation of the references to colour in this figure legend, the reader is referred to the web version of this article.)

these, four were MGC<sup>3</sup> PCEs, meaning ~6% of the 68 known PCEs in the region were detected. Region A also contains four PCE-dense subregions: A<sub>1</sub>-A<sub>4</sub> (Fig. 6).

**Region B:** There were 2380 positive outputs from region B, with 44 true positives (1.85%). Of the 44 true positives, 10 were MGC<sup>3</sup> PCEs, meaning ~7% of the 152 known PCEs were detected. Region B also contains four PCE-dense subregions: B<sub>1</sub>-B<sub>4</sub> (Fig. 7).

**Region C:** CaveFinder output 3950 positive detections from region C, only 17 of which were deemed true positives (0.43%). Six of the 89 MGC<sup>3</sup> PCEs were correctly identified (~7%). Region C also contains two

PCE-dense subregions: C<sub>1</sub> and C<sub>2</sub> (Fig. 8).

**Region D:** Region D produced 621 positive detections; however, no detections were deemed true positives.

**Region E:** 1402 positive detections were identified in region E, 13 of which were deemed true positives (0.93%). Four of these were MGC<sup>3</sup> PCEs, meaning 12.5% of the 32 MGC<sup>3</sup> PCEs in this region were correctly identified. Region E also contains two PCE-dense subregions: E<sub>1</sub> and E<sub>2</sub> (Fig. 9).

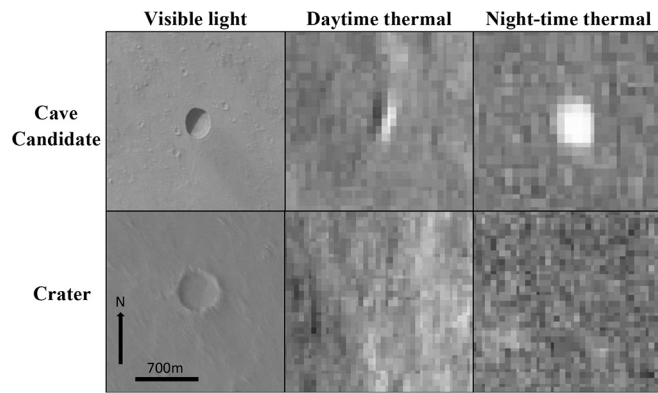


**Fig. 11.** The use of thermal imaging to verify PCEs. During the day, large caves have a cool thermal signature (represented by darker pixels) whereas at night they have a warmer thermal signature (represented by whiter pixels). Non-cave features, such as craters, tend to either have one or none of the aforementioned thermal signatures. Thermal images were captured on the THEMIS IR Mosaics (Edwards et al., 2011).

## 4. Discussion

### 4.1. PCEs of specific interest

Of the 61 newly detected PCEs, four are highlighted for having specific traits that warrant further exploration (included in Table 2). These PCEs, along with a handful of other examples, have been informally assigned names for ease of reference, following previous convention (Cushing et al., 2007). ‘Emily’ is an APC located at  $-1020$  m on the northern flank of Elysium Mons. Geographically, Emily is the lowest altitude PCE identified in this survey. This is significant because this altitude’s denser atmosphere allows for increased generation of lift, aiding the landing of landers and rovers with parachutes as well as allowing for exploration via drone flight (Ata, 2021). Additionally, the denser atmosphere at Emily’s altitude would facilitate future human habitation. Five other MGC<sup>3</sup> PCEs exist within 15 km of Emily, making this a promising region for targeted cave exploration. The PCE is also significantly larger than the five surrounding PCEs, potentially increasing accessibility.

At 700 m in diameter ‘Marvin’, located northeast of Arsia Mons, is the largest PCE identified in this survey. The entrance’s size could assist the landing of robotics, because precision landings are more complex for smaller cave targets (Cushing, 2015). Further research of Marvin will also improve understanding of how large cave entrances can form under Mars’ gravity.

‘Frankie’ is an excellent example of an APC that appears to be partially filled by wind-blown dust. Located on the flanks of Arsia Mons, Frankie is part of an 18 km chain of pit collapses, most of which also appear to be partially filled. This may make them more accessible by vehicle, if ramp-like features have formed (Cushing, 2012), such as the one formed at the southern part of Frankie’s entrance.

‘Steve’ is located on the flank of Elysium Mons and is part of a 100 km-long linear geological feature. The MGC<sup>3</sup> PCE ‘CC0012’ is located along the same linear feature, 22 km to the SE. Multiple sections of the feature remain covered for kilometres, raising the potential for extensive exploration. However, the feature is associated with the Zephyrus fossae, and has formed radial to the volcano Elysium Mons, suggesting this could be a type of graben formed at the edge of a lava field rather than a lava tube collapse. This highlights the possibility that some of the new PCEs are the result of processes other than lava tubes. Although the likelihood of a substantial cave is reduced in these instances, some passage or chambers may still exist, and we include these identifications for the sake of completeness. Further research is required to determine if sub-surface cave systems are associated with fossae or other similar

features.

### 4.2. PCE-dense subregions

Twelve PCE-dense subregions are identified as part of this study, comprising mostly MGC<sup>3</sup> and some newly identified PCEs (Table 3). They represent particularly important areas for further exploration due to the high abundance of PCEs located within them. The limited range of current Martian rovers (travelling a maximum of 100 m per day), and the associated costs and logistical challenges faced, mean only a handful of rover missions have been undertaken. Hence, regions with high concentrations of closely spaced PCEs, such as these, are desirable because they could facilitate multi-cave exploration as part of single rover missions. They would also benefit future crewed missions, with multiple caves allowing for the construction of multiple shelters, enabling wider exploration. Region B<sub>2</sub>, the largest of these PCE-dense subregions, contains both the highest number of newly identified PCEs, and the largest overall number of PCEs. (Table 3). Located on the NE flanks of Arsia Mons, the region has experienced high volcanic activity and has well-preserved and abundant lava flows (Mouginis-Mark and Rowland, 2008), consistent with the presence of numerous lava tubes.

Studying PCEs identified in region B<sub>2</sub> will provide insight into the types of eruptions that occurred during the late Amazonian period (the last few millions of years), helping to detangle Tharsis regional development and refine the overall geological framework of Martian volcanism (Bleacher et al., 2007). Furthermore, studying the wide variety of PCE types and sizes in this subregion (Fig. 10) would also provide insight into the different mechanisms of cave formation on Mars.

The subregion avoids extreme seasonal insolation variations due to its proximity to the equator, thus providing a secure solar energy supply for both autonomous vehicles and future human shelters (German Aerospace Centre, 2018). The Tharsis region itself is also conducive to ice cave formation (Williams et al., 2010), increasing the chances of PCEs in subregion B<sub>2</sub> harbouring life, as well as providing a potential water supply for crewed missions.

However, if life is detected in these PCEs, human access would necessarily become restricted to prevent contamination (Race et al., 2005). Thorough remote robotic evaluation for cave-based bio-signatures is therefore required prior to crewed missions. The eastern portion of the region is relatively flat, remaining at a near-constant elevation for 100 km east to west. However, the gradient steepens beyond this, restricting accessibility with current rover technologies (German Aerospace Centre, 2018). Hence, advancements in robotic capabilities are also required prior to further exploring this subregion.

### 4.3. Thermal imagery

Satellite imagery alone cannot confirm the presence of void spaces extending beneath the surface from PCEs (Cushing, 2015). One method to improve confidence in the identified PCEs is through thermal imaging (Fig. 11). The subsurface voids associated with cave entrances produce unique thermal signatures compared to their surroundings, due to the lack of insolation they receive (Wynne et al., 2008). They experience less temperature variation, making them appear warmer at night and cooler during the day (Cushing et al., 2007). This property is theoretically quantifiable using the Thermal Emissions Imaging System (THEMIS) onboard the Odyssey Orbiter (Edwards et al., 2011). Most large APCs and irregular pits identified in this survey appear to have thermal signatures consistent with cave entrances. However, the resolution of THEMIS only allows for visualisation of larger PCEs this way, and so was not successful on smaller PCEs. Furthermore, not all cave entrances give off distinct thermal signatures (Jung et al., 2014) and other surface features, such as deep craters, can also produce similar signatures, adding to uncertainty inherent with this technique.

To quantify the uncertainty in each validated PCE, new PCEs are

catalogued with an associated confidence between one and three, where one is the highest confidence (Supplementary Table 1). PCEs with multiple features indicative of a cave, such as thermal signatures, associated lava tubes, and overhanging rims are assigned a confidence of one. PCEs that visibly resemble known PCEs and are potentially linked to other MGC<sup>3</sup> PCEs but lack features such as thermal signatures, or are poorly resolved, are assigned a confidence of two. PCEs that resemble MGC<sup>3</sup> PCEs but are isolated from other entrances and lack features such as thermal signatures are assigned a confidence of three.

## 5. Conclusion

CaveFinder has identified 61 new PCEs across four of the five regions surveyed. Four PCEs are highlighted for having specific qualities that make them interesting for further research, including Marvin, the largest PCE identified, as well as Emily, whose low altitude could enable surveillance by drone. Twelve PCE-dense subregions are also identified, which could facilitate rapid exploration due to the proximity and abundance of PCEs. Whilst CaveFinder was successful in identifying new PCEs, analysis of the network's performance shows most of the smaller PCEs identified in the survey were located in channels thought to have enhanced the network's ability to identify them (see Supplementary Information). This suggests CaveFinder's ability to identify lone small cave types, such as skylights and pinholes is more limited.

CaveFinder achieved a test accuracy of 77% and a specificity of 100% indicating that the network is conservative with positive predictions (see Supplementary Information). Following survey data input, 0.70% of images triggered a positive detection, further emphasising CaveFinder's conservative approach. Of these positive detections, only 0.78% were found to contain a PCE. However, this result implies CaveFinder does perform better than random search, with 7.04% of the 341 MGC<sup>3</sup> PCEs present in the survey regions being correctly identified. Despite this, CaveFinder is still not considered appropriate for detection on a planet-wide scale, due to the high number of false positive outputs requiring manual assessment. However, it could prove effective in smaller regions perhaps already known to contain PCEs.

Increasing the size of the training dataset is one method that would likely improve CaveFinder's performance. This could be achieved through the use of computer generated imagery (CGI) or through higher levels of image zoom to capture more true positive PCE examples. Other suggestions for improvement include utilising thermal imagery alongside VLI within the network itself, as well as using higher resolution imagery from the Mars NeMo Orbiter (see Supplementary Information). Overall, this survey's findings indicate that, with these additions, machine learning has a great potential to advance remote cave detection, which is key to future Martian exploration.

## CRedit authorship contribution statement

**Thomas H. Watson:** Data curation, Formal analysis, Investigation, Methodology, Project administration, Resources, Software, Visualization, Writing – original draft, Writing – review & editing. **James U.L. Baldini:** Conceptualization, Supervision, Validation, Writing – review & editing.

## Declaration of competing interest

The authors declare that they have no known competing financial interests or personal relationships that could have appeared to influence the work reported in this paper.

## Data availability

All data is attached in the SOM. please contact if further assistance is required.

## Acknowledgements

Thanks to Edward Morris for inspiring the use of Keras and Automated python scripts. We thank Emily Binns, Gabriele Morra and the anonymous reviewers for helpful comments that greatly improved the manuscript.

## Appendix A. Supplementary data

Supplementary data to this article can be found online at <https://doi.org/10.1016/j.icarus.2024.115952>.

## References

- Allred, K., Allred, C., 1997. Development and morphology of Kazumura cave, Hawaii. *J. Cave Karst Stud.* 59 (2), 67–80.
- Aprovitola, A., Medugno, F., Pezzella, G., Luspa, L., Viviani, A., 2022. Lifting entry analysis for manned Mars exploration missions. In: *Hypersonic Vehicles - Applications, Recent Advances, and Perspectives*.
- Ata, O.W., 2021. Aerodynamic performance of advanced ingenuity and dragonfly drones for future space missions to Mars and Titan. In: *2021 4th International Symposium on Advanced Electrical and Communication Technologies (ISAECT)*.
- Barton, H., 2006. Introduction to cave microbiology: a review for the non-specialist. *J. Cave Karst Stud.* 68 (2), 43–54.
- Biswal M, M.K., Kumar, R., 2021. Conceptual Design of a Mars Sample Return Architecture through Solar Montgolfier Powered Mars Ascent and Descent Mechanism. In: *Space Infrastructure and Miscellaneous Exploration Missions II*.
- Bleacher, J.E., Greeley, R., Williams, D.A., Werner, S.C., Hauber, E., Neukum, G., 2007. Olympus Mons, Mars: inferred changes in late Amazonian aged effusive activity from lava flow mapping of Mars express high resolution stereo camera data. *J. Geophys. Res.* 112 (E4).
- Boston, P.J., 2004. Extraterrestrial Subsurface Technology Test Bed: Human Use and Scientific Value of Martian Caves. *AIP Conference Proceedings*.
- Boston, P.J., Spilde, M.N., Northrup, D.E., Melim, L.A., Soroka, D.S., Kleina, L.G., Lavoie, K.H., Hose, L.D., Mallory, L.M., Dahm, C.N., Crossey, L.J., Schelble, R.T., 2001. Cave biosignature suites: microbes, minerals, and Mars. *Astrobiology* 1 (1), 25–55.
- Carr, M.H., 1973. Volcanism on Mars. *J. Geophys. Res.* 78 (20), 4049–4062.
- Carr, M.H., Head III, James W., 2010. Geologic history of Mars. *Earth Planet. Sci. Lett.* 294, 185–203.
- Chollet, F., 2015. Keras [online] Available at. <https://github.com/fchollet/keras>.
- Christensen, P.R., Engle, E., Anwar, S., Dickenshied, S., Noss, D., Gorelick, N., Weiss-Malik, M., 2022. JMARS – A Planetary GIS. <http://adsabs.harvard.edu/abs/2009AGUFMIN22A.06C>.
- Cushing, G., 2012. Candidate cave entrances on Mars. *J. Cave Karst Stud.* 74 (1), 33–47.
- Cushing, G., 2015. Mars Global Candidate cave Catalogue PDS4 Archive Bundle. PDS Cartography and Imaging Sciences Node (IMG).
- Cushing, G.E., Titus, T.N., Wynne, J.J., Christensen, P.R., 2007. THEMIS observes possible cave skylights on Mars. *Geophys. Res. Lett.* 34 (17).
- Cushing, G.E., Okubo, C.H., Titus, T.N., 2015. Atypical pit craters on Mars: new insights from THEMIS, CTX, and HiRISE observations. *J. Geophys. Res. Planet* 120 (6), 1023–1043.
- Dede, G., 2022. Performance-driven design methodology for habitation shell design in extreme conditions on Mars. *Front. Archit. Res.* 11 (2), 224–238. <https://doi.org/10.1016/j.foar.2021.10.005>.
- Dickson, L., Kerber, A., Fassett, C., Ehlmann, B., 2018. A global, blended CTX mosaic of mars with vectorized seam mapping: a new mosaicking pipeline using principles of non-destructive image editing. In: *Division of Geological and Planetary Science, California Institute of Technology, 1200 E California Blvd, MC 150–21*.
- Edwards, C.S., Christensen, P.R., Hill, J., 2011. Mosaicking of global planetary image datasets: 2. Modeling of wind streak thicknesses observed in thermal emission imaging system (THEMIS) daytime and nighttime infrared data. *J. Geophys. Res.* E10. E10005.
- German Aerospace Centre, 2018. The landing site for the InSight mission [online] Available at. [https://www.dlr.de/content/en/images/2018/2/the-landing-site-for-the-insight-mission-in-elysium-planitia\\_30417.html](https://www.dlr.de/content/en/images/2018/2/the-landing-site-for-the-insight-mission-in-elysium-planitia_30417.html).
- Graham, B., 2015. Sparse 3D convolutional neural networks. *arXiv:1505.02890*.
- Gunn, J., 2004. *Encyclopedia of Caves and Karst Science*. Fitzroy Dearborn, New York: London.
- Haruyama, J., Hioki, K., Shiro, M., Morota, T., Hiesinger, H., van der Bogert, C.H., Miyamoto, H., Iwasaki, A., Yokota, Y., Ohtake, M., Matsunaga, T., 2009. Possible lunar lava tube skylight observed by SELENE cameras. *Geophys. Res. Lett.* 36 (21).
- Hodges, C.A., Moore, H.J., 1994. *Atlas of Volcanic Landforms on Mars*. U.S. G.P.O.; Denver, Co, Washington.
- Husseini, A.M.A., Apeldoorn, J., Ashford, K.L., Bennell, K.M., de Carufel, G., Haider, O., Hirmer, T., 2009. The role of caves and other subsurface habitats in the future exploration of Mars. In: *International Space University Space Studies Program 2009*.
- Jung, J., Yi, Y., Kim, E., 2014. Identification of Martian cave skylights using the temperature change during day and night. *J. Astron. Space Sci.* 31 (2), 141–144.
- Kemp, S., 2019. Volcanic rock caves. In: *Encyclopedia of Caves*, 3, pp. 1118–1127.
- Leone, G., 2014. A network of lava tubes as the origin of Labyrinthus Noctis and Valles Marineris on Mars. *J. Volcanol. Geotherm. Res.* 277, 1–8.

- Léveillé, R.J., Datta, S., 2010. Lava tubes and basaltic caves as astrobiological targets on Earth and Mars: a review. *Planet. Space Sci.* 58 (4), 592–598.
- Mikołajczyk, A., Grochowski, M., 2018. Data augmentation for improving deep learning in image classification problem, pp. 117–122. <https://doi.org/10.1109/IIPHDW.2018.8388338>.
- Mouginis-Mark, P.J., Rowland, S.K., 2008. Lava flows at Arsia Mons, Mars: insights from a graben imaged by HiRISE. *Icarus* 198 (1), 27–36.
- Muralidhar, K.S.V., 2021. Learning Curve to identify Overfitting and Underfitting in Machine Learning [online] Medium. Available at. <https://towardsdatascience.com/learning-curve-to-identify-overfitting-underfitting-problems-133177f38df5>.
- Murchie, S., Arvidson, R., Bedini, P., Beisser, K., Bibring, J.-P., Bishop, J., Boldt, J., Cavender, P., Choo, T., Clancy, R.T., Darlington, E.H., Des Marais, D., Espiritu, R., Fort, D., Green, R., Guinness, E., Hayes, J., Hash, C., Heffernan, K., Hemmler, J., 2007. Compact reconnaissance imaging spectrometer for Mars (CRISM) on Mars reconnaissance orbiter (MRO). *J. Geophys. Res.* 112 (E5).
- Nagle-McNaughton, T., McClanahan, T., Scuderi, L., 2020. PlaNet: a neural network for detecting transverse Aeolian ridges on Mars. *Remote Sens.* 12 (21), 3607.
- Neukum, G., Jaumann, R., Hoffmann, H., Hauber, E., Head, J.W., Basilevsky, A.T., Ivanov, B.A., Werner, S.C., van Gasselt, S., Murray, J.B., McCord, T., 2004. Recent and episodic volcanic and glacial activity on Mars revealed by the high-resolution stereo camera. *Nature* 432 (7020), 971–979.
- O'Shea, K., Nash, R., 2015. An Introduction to Convolutional Neural Networks. *arXiv:1511.08458*.
- Palafox, L.F., Hamilton, C.W., Scheidt, S.P., Alvarez, A.M., 2017. Automated detection of geological landforms on Mars using convolutional neural networks. *Comput. Geosci.* 101, 48–56.
- Petrovsky, A., Kalinov, I., Karpyshev, P., Tsetseroukou, D., Ivanov, A., Golkar, A., 2022. The two-wheeled robotic swarm concept for Mars exploration. *Acta Astronaut.* 194, 1–8.
- Phillips, R.J., 2001. Ancient geodynamics and global-scale hydrology on Mars. *Science* 291 (5513), 2587–2591.
- Quaide, W.L., Oberbeck, V.R., 1969. Geology of the Apollo landing sites. *Earth Sci. Rev.* 5 (4), 255–278.
- Race, M., Criswell, M., Rummel, J., 2005. Planetary protection issues in the human exploration of Mars. In: Technical Paper arising from the International Conference On Environmental Systems. <https://doi.org/10.4271/2003-01-2523>.
- Rossi, A.P., van Gasselt, S., 2010. Geology of Mars after the first 40 years of exploration. *Res. Astron. Astrophys.* 10 (7), 621–652.
- Saha, S., 2018. A Comprehensive Guide to Convolutional Neural Networks — The ELI5 Way. Towards Data Science.
- Sauro, F., Pozzobon, R., Massironi, M., De Berardinis, P., Santagata, T., De Waele, J., 2020. Lava tubes on Earth, Moon and Mars: a review on their size and morphology revealed by comparative planetology. *Earth Sci. Rev.* 209, 103288.
- Shozaki, H., Sekine, Y., Guttenberg, N., Komatsu, G., 2022. Recognition and classification of Martian chaos terrains using imagery machine learning: a global distribution of chaos linked to groundwater circulation, catastrophic flooding, and magmatism on Mars. *Remote Sens.* 14 (16), 3883. <https://doi.org/10.3390/rs14163883>.
- Simonyan, K., Zisserman, A., 2014. Very Deep Convolutional Networks for Large Scale Image Recognition. <https://arxiv.org/abs/1409.1556>.
- Wagner, R.V., Robinson, M.S., 2014. Distribution, formation mechanisms, and significance of lunar pits. *Icarus* 237, 52–60.
- Wang, H., Jiang, J., Zhang, G., 2018. CraterIDNet: an end-to-end fully convolutional neural network for crater detection and identification in remotely sensed planetary images. *Remote Sens.* 10 (7), 1067.
- Williams, K.E., McKay, C.P., Toon, O.B., Head, J.W., 2010. Do ice caves exist on Mars? *Icarus* 209 (2), 358–368.
- Wilson, L., Head, J.W., 1994. Mars: review and analysis of volcanic eruption theory and relationships to observed landforms. *Rev. Geophys.* 32 (3), 221.
- Wynne, J.J., Titus, T.N., Chong Diaz, G., 2008. On developing thermal cave detection techniques for earth, the moon and mars. *Earth Planet. Sci. Lett.* 272 (1–2), 240–250.